JOURNAL OF AIRCRAFT
Vol. 48, No. 2, March–April 2011

Three-Dimensional Effects on Sliding and Waving Wings

A. R. Jones,* C. W. Pitt Ford,* and H. Babinsky†
University of Cambridge, Cambridge, England CB2 1PZ, United Kingdom

DOI: 10.2514/1.C031184

Like large insects, micro air vehicles operate at low Reynolds numbers $\mathcal{O}(1,000-10,000)$ in a regime characterized by separated flow and strong vortices. The leading-edge vortex has been identified as a significant source of high lift on insect wings, but the conditions required for the formation of a stably attached leading-edge vortex are not yet known. The waving wing is designed to model the translational phase of an insect wing stroke by preserving the unsteady starting and stopping motion as well as three-dimensionality in both wing geometry (via a finite-span wing) and kinematics (via wing rotation). The current study examines the effect of the spanwise velocity gradient on the development of the leading-edge vortex along the wing as well as the effects of increasing three-dimensionality by decreasing wing aspect ratio from four to two. Dye flow visualization and particle image velocimetry reveal that the leading-edge vortices that form on a sliding or waving wing have a very high aspect ratio. The structure of the flow is largely two-dimensional on both sliding and waving wings and there is minimal interaction between the leading-edge vortices and the tip vortex. Significant spanwise flow was observed on the waving wing but not on the sliding wing. Despite the increased three-dimensionality on the aspect ratio 2 waving wing, there is no evidence of an attached leading-edge vortex and the structure of the flow is very similar to that on the higher-aspect-ratio wing and sliding wing.

Nomenclature

c = wing chord, m
Re = Reynolds number, Uc/ν
U = local freestream, m s^{-1}
x = distance traveled, m
α = angle of attack
γ = scalar measure of fluid rotation
θ = wing stroke angle, deg
ω = angular velocity, rad s^{-1} or vorticity, m^2 s^{-1}

I. Introduction

MICRO air vehicle (MAV) development has renewed interest in unsteady low Reynolds number aerodynamics. These small vehicles operate at Reynolds numbers $\mathcal{O}(1,000-10,000)$, in the same flight regime as large insects. Natural flight in this low Reynolds number regime is primarily flapping wing flight and it is generally thought that unsteady aerodynamic phenomena are required to achieve the necessary lift coefficients.

Zoologists have identified the leading-edge vortex (LEV) on flapping insect wings as one of the high lift mechanisms that allows for both lift generation and flight control [1–6]. This vortex, which persists through each insect wing half-stroke, is produced and fed by leading-edge separation [7] but there is some uncertainty about the mechanism that stabilizes it. Lentink and Dickinson [8] have likened the flow on a revolving wing to Ekman pumping and propose that LEV stability is influenced by the Rossby number (Ro), the ratio of the inertial force to the Coriolis force in a rotating flow, and not the Reynolds number. At a low Rossby number, Coriolis forces dominate, whereas at high Ro, inertial forces are dominant. Lentink and Dickinson suggest that revolving wings operating at a low Ro mediate compact and stable LEVs, whereas the LEV is unstable for translating wings which have no Coriolis acceleration and therefore $Ro = \infty$. Other authors [3,7,9,10] propose that the LEV is stabilized by the spanwise vorticity transport that accompanies wing rotation. Propeller-like wing rotation induces a spanwise velocity gradient which may drive spanwise vorticity transport that locally limits the size of the LEV and prevents it reaching the critical size at which it becomes unstable.

In a two-dimensional flow without wing rotation, the two unsteady aerodynamic mechanisms of primary interest are the Wagner effect and delayed stall. The Wagner effect accounts for the delay in the growth of circulation about a wing set in motion from rest at a low angle of incidence. In physical terms, downwash induced by the starting vortex lowers the effective angle of incidence, reducing the lift generated. Circulation asymptotically approaches the steady state value, reaching approximately 90% after six chords of travel [11–13]. Delayed stall is a well-known effect on that can result in high lift for short timescales. When a wing at high incidence, above the static stall angle, is accelerated through a fluid it produces very high lift for approximately four chord lengths as a vortex forms on the leading edge. This vortex soon sheds and is convected over the suction surface of the wing [14]. While the wing is accelerating other aerodynamic forces may be produced due to added mass and the growth and shedding of a boundary layer.

Several experimental studies have been conducted that aim to simplify the complex kinematics of insect wing motion. Among the simplest is the impulsively started flat plate, a problem which has received considerable attention on account of its fundamental nature. An impulsively started flat plate at high incidence and low Reynolds number models the translational stages of an insect's flapping cycle, preserving the geometric three-dimensionality of the flow via a finite-span wing but neglecting the three-dimensionality of the wing kinematics, i.e., wing rotation. Beckwith and Babinsky's [15] experimental study of an impulsively started flat plate at $\alpha = 5$ and $\alpha = 15$ deg and $Re = 60,000$ has shown that for angles of incidence greater than the steady state stall angle, delayed stall causes an increase in lift during the first chord of travel, whereas at angles less than the steady state stall angle the Wagner effect dominates and there is a lift deficiency early in the wing motion relative to the steady state case.

The waving wing experiment was designed to model the translational phase of the insect wing stroke with a simple flowfield while preserving wing rotation and three-dimensionality in both geometry and kinematics. Previous experiments [16] have shown that the waving wing produces a transient lift peak due to the growth and shedding of a LEV. Vortices continue to form and shed and the lift

Received 20 July 2010; revision received 2 October 2010; accepted for publication 5 October 2010.

*Research Student, Aerodynamics Laboratory, Department of Engineering, Trumpington Street. Student Member AIAA.
†Reader in Aerodynamics, Aerodynamics Laboratory, Department of Engineering, Trumpington Street. Senior Member AIAA.

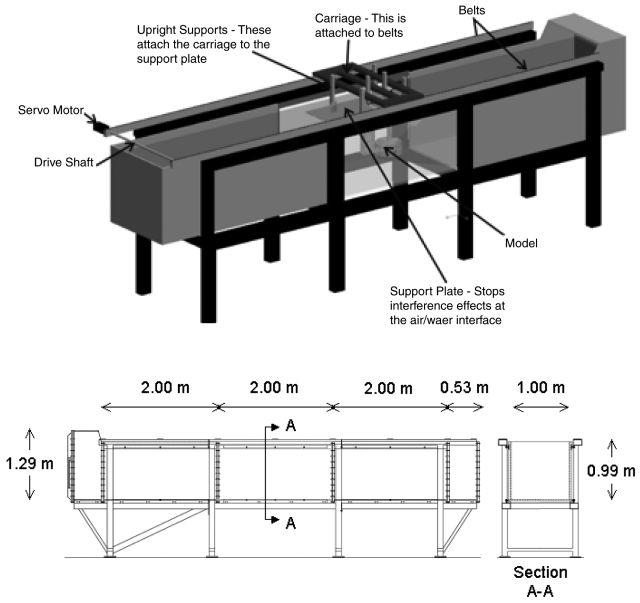

Fig. 1 CUED towing tank.

force becomes quasi steady as a trail of vortices extends downstream over the wing. Wing kinematics can affect the timing and height of the lift peak if the wing acceleration is low [16]. At low wing accelerations the force history of the waving wing is similar to that of Beckwith and Babinsky's impulsively started flat plate. Previously [17], it has been found that the fundamental structure of the flow field did not change significantly at angles of attack between 15 and 45 deg.

The current work assesses the stability of the LEV using the impulsively started flat plate and waving wing setups. The aim is to offer further insight into the unsteady mechanisms that affect lift generation on finite wings at low Reynolds numbers to determine whether an unsteady flapping motion could offer increased lift for MAV applications. Unsteadiness and three-dimensionality in both wing geometry and kinematics are thought to be important for the development of a stably attached LEV. Previous work [18] focused on characterizing the fundamental structure of the flowfield around a waving wing. The research presented here extends this work to investigate the relative three-dimensionality of the flowfield around a wing in pure translation and a wing undergoing rotation. Using both the sliding and waving wing setups, flow three-dimensionality is incrementally introduced via changes in both wing kinematics and geometry. The primary questions addressed here are: how does the fundamental structure of the flow change when a wing undergoes rotation rather than pure translation? How does the spanwise velocity gradient affect the development of the LEV along the waving wing? Can the unstable LEV previously observed on the waving wing be stabilized by increasing the three-dimensionality of the flow?

II. Experimental Methods

A. Experimental Setup

Experiments were performed in the Cambridge University Engineering Department (CUED) towing tank, shown in Fig. 1. Water provides an optimal environment for high resolution data

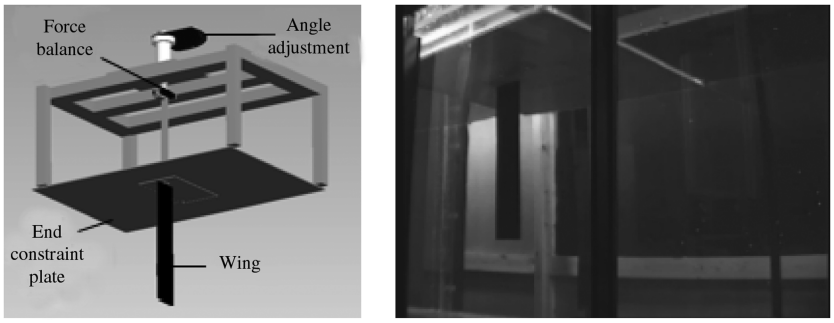

a) Schematic of the sliding wing

b) Photograph of the wing suspended from the carriage in the towing tank

Fig. 2 Sliding wing setup, from [22].

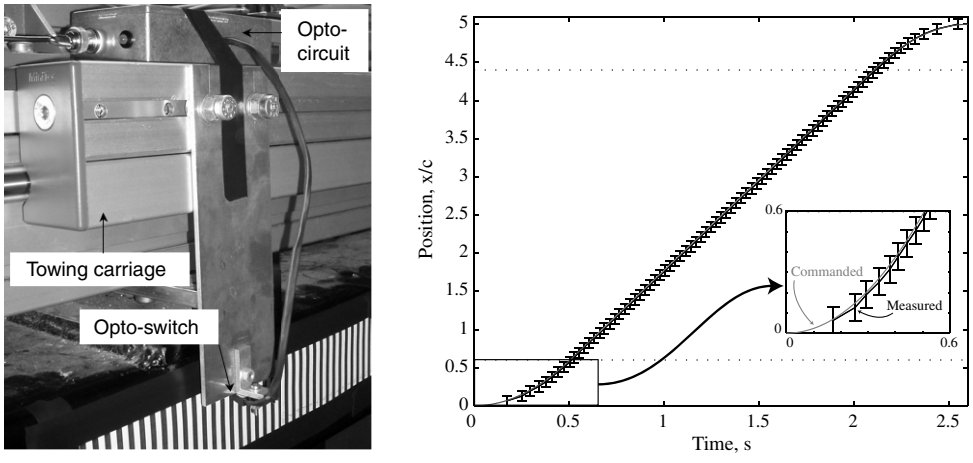

a) Photograph of the opto-switch showing the light and dark bands on the side of the tank

b) Commanded and measured position-time graph

Fig. 3 Position of the carriage is verified using a reflective optoswitch.

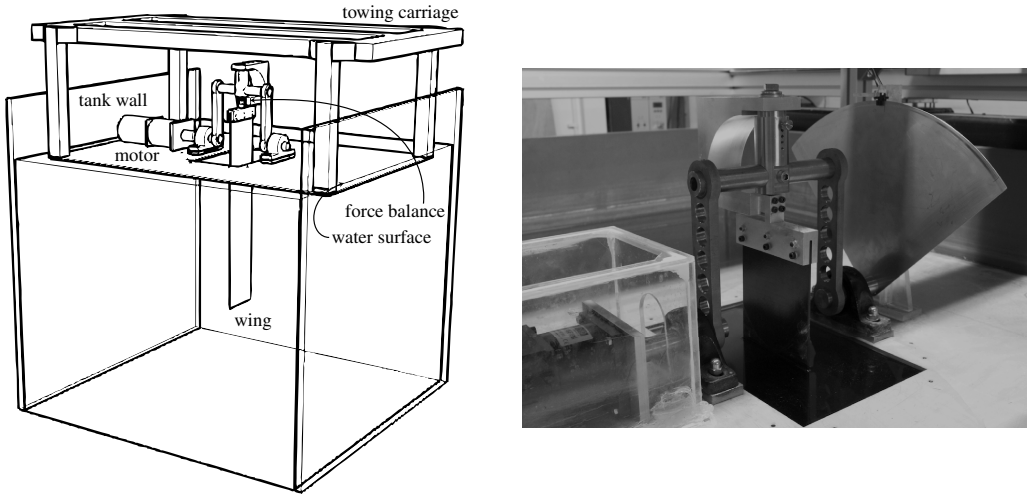

Fig. 4 Waving wing setup.

acquisition in both time and space because it is possible to achieve the required Reynolds numbers with relatively slow motions and a large model. Additionally, towing the model through a quiescent fluid provides good flow quality and low freestream turbulence. The towing tank is 7 m long and has a 1 m × 1 m cross section with a central 2 m long Perspex test section and a glass window on one end. The computer-controlled carriage is capable of speeds up to 4.75 m s^{-1} ±0.25%.

Three flat plate wings were tested, one sliding wing made of aluminum with an aspect ratio of four and a chord of 0.120 m and two waving wings made of carbon fiber with an aspect ratio of four and two (or eight and four if the end plate is taken as an image plane) and a chord length of 0.125 m. All of the wings have rounded edges and are 2.5% thick. The angle of incidence can be varied between 0 and 45 deg in 5 deg increments.

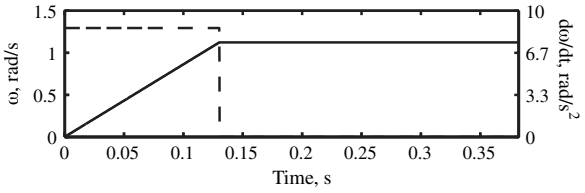

Fig. 5 Commanded wing kinematics for first quarter-stroke accelerating to $Re = 60,000$ over $0.25c$: angular velocity (solid) and acceleration (dashed) as a function of time.

1. Sliding Wing

A schematic and photograph of the sliding wing is shown in Fig. 2. The wing is mounted at its root on a large end plate in order to remove free-surface effects, doubling the effective aspect ratio. Using the computer-controlled towing carriage, the sliding wing undergoes constant acceleration from rest to its final speed over a distance of $0.08c$. Thereafter, the wing travels at constant speed. A Reynolds number of 10,000 corresponds to a velocity of 0.10 m s^{-1}.

The wing velocity profile is verified using a reflective optoswitch mounted on the side of the tow-tank as shown in Fig. 3. Light and dark bands of width 4 mm are fixed to the side of the tank and as the carriage moves over the bands the opto-output switches. This signal is then processed to determine the position and velocity of the carriage. An example of the position-time profile is shown in Fig. 3b for acceleration to $Re = 30,000$ over 0.6 chord lengths. The error bars of 8 mm ($c/15$) correspond to the spacing between consecutive dark bands. The dashed lines represent the point at which the carriage stops ($0.6c$) and starts ($4.4c$) accelerating. An inset is shown of the position profile while the wing is accelerating. Using particle image velocimetry (PIV) images, the amplitude of the wing vibration at 3/4 span on the aspect ratio 2 wing was found to be approximately 0.3 mm.

2. Waving Wing

For the waving wing experiments the towing carriage remains stationary and the wing waves through the end plate. A sketch and

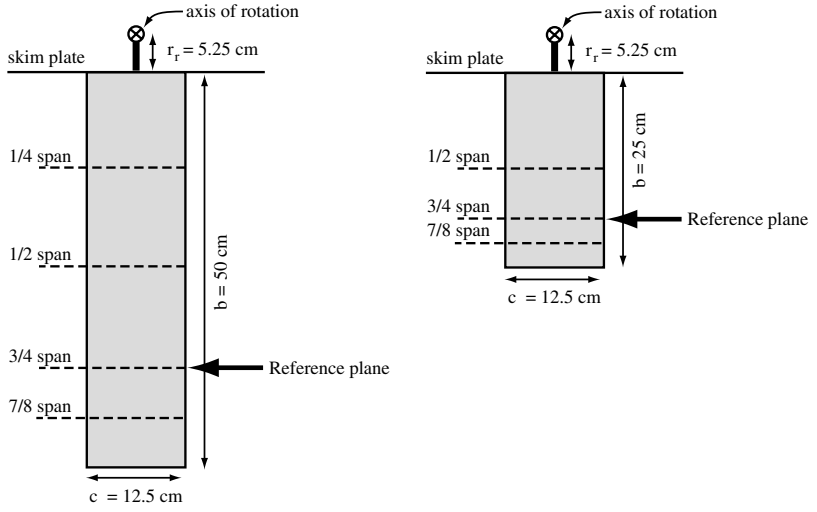

a) Aspect ratio 4 wing **b) Aspect ratio 2 wing**

Fig. 6 Schematic of the waving wings.

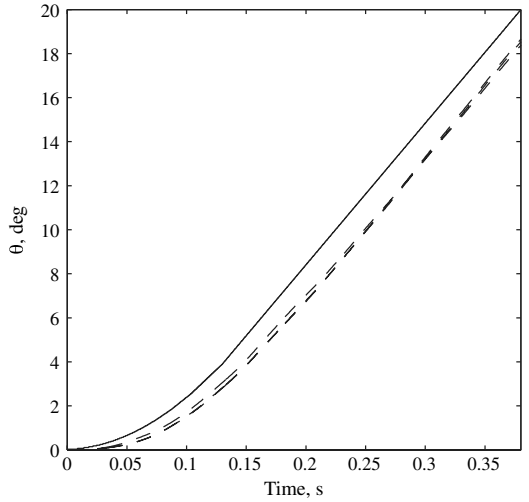

Fig. 7 Commanded (solid) and measured (dashed) wing position for the first quarter of the wing stroke at $Re = 60,000$.

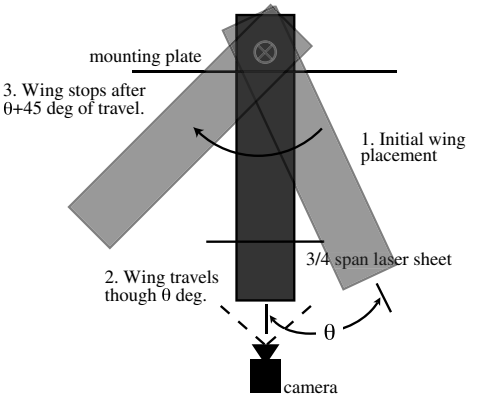

Fig. 8 Chordwise PIV setup.

photograph of the waving wing mechanism is shown in Fig. 4. The entire setup is shown suspended from the towing tank carriage on four vertical struts and the Perspex sides and water volume of the tank are shown to provide a sense of scale.

The waving motion is controlled by a servomotor and gearbox programmable through LabView and a slotted optical switch is mounted near one end of the axle to confirm wing position. The distance from the wing root (defined as the bottom of the skim plate when the wing is vertical) to the axis of rotation is 10% of the wing span. An 85 deg wing stroke is equivalent to 5.07 chord lengths of travel at 3/4 span of the aspect ratio 4 wing. Blockage of the towing tank is 5.5% at a 45 deg angle of attack. The angle of attack is selectable from 0 to 45 deg in 5 deg increments and is accurate to within 1/60 of a degree. The stepper motor is capable of commanding the wing position to within 0.2 deg.

The wing stroke was programmed using a linear velocity profile in time as shown in Fig. 5. The wing was accelerated such that it reached its maximum velocity after 0.25 chord lengths of travel at 3/4 span and the velocity profile was symmetric such that the wing decelerated in the same way before reaching the end of the stroke. The maximum velocity was chosen as that which gives the target local wing Reynolds number at the 3/4 span reference plane (Fig. 6).

The wing position as a function of time was measured using a high speed camera. Images were acquired at 2 kHz and the angular position of the wing computed for three runs. Figure 7 shows the angular wing position as a function of time for the wing at a 45 deg angle of attack and $Re = 60,000$. There are three sets of dashed lines representing the three runs measured. Once the wing has reached its constant velocity there is a 10% error in position or a 3.5% error in angular velocity. The error in wing position appears to be due to a slight delay in the start of the wing motion, thus despite the offset the wing position at a given point in time is precise.

B. Particle Image Velocimetry

PIV was performed using a LaVision FlowMaster 4S DPIV with a high resolution high speed camera capable of up to 1000 frames per second at a resolution of 1024 × 1024 pixels and a Nd:YLF double cavity laser.

To obtain PIV data for chordwise slices of the waving wing the laser sheet was oriented horizontally and entered the tank through the side wall. The camera was placed below the tank as shown in Fig. 8. Images were taken at 1/4, 1/2, 3/4, and 7/8 span throughout the wing stroke. Each case was repeated between 5 and 50 times though analysis of early data demonstrated that 5 runs was sufficient in all cases and the figures presented here represent five phase-averaged runs.

Vestosint 7182 particles with a specific gravity of 1.02 and mean diameter of 30 microns were used to seed the flow. Because of

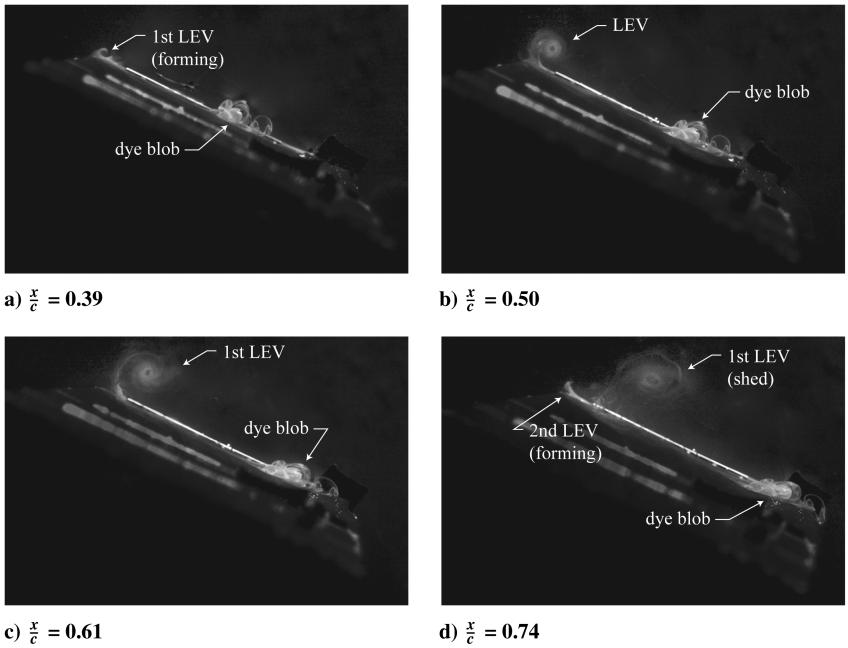

a) $\frac{x}{c}$ = 0.39 **b) $\frac{x}{c}$ = 0.50**

c) $\frac{x}{c}$ = 0.61 **d) $\frac{x}{c}$ = 0.74**

Fig. 9 Chordwise view of dye flow visualization at 1/2 span on the sliding wing at $Re = 10,000$, $\alpha = 25$ deg.

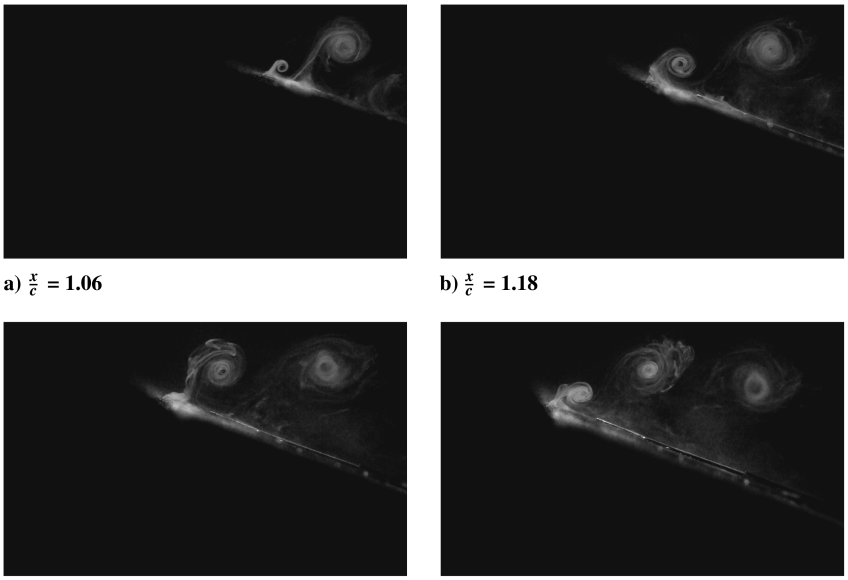

a) $\frac{x}{c}$ = 1.06 b) $\frac{x}{c}$ = 1.18

c) $\frac{x}{c}$ = 1.31 d) $\frac{x}{c}$ = 1.45

Fig. 10 Chordwise view of dye flow visualization at 3/4 span on the sliding wing at $Re = 10,000$, $\alpha = 25$ deg.

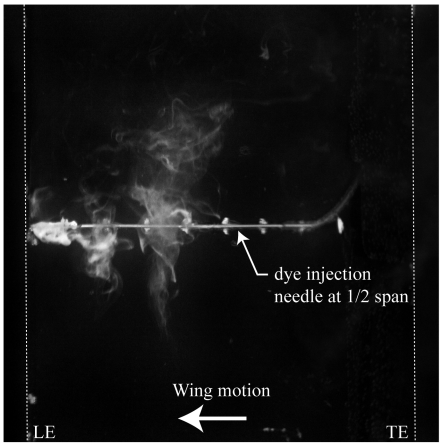

Fig. 11 Spanwise view of dye injected at 1/2 span on the sliding wing after 4.55 chord lengths of travel. Shed vortices are visible at 0.20*c* and 0.35*c* from the leading edge.

diffraction, the particle diameter in the images was between 2 and 3 pixels. Images were taken at frame rates between 50 and 750 Hz at a resolution of 1024 × 1024 pixels with a 35 × 35 cm field of view. Frame rates were chosen for a 3 to 5 pixel particle displacement within image pairs. PIV images were processed in two passes with interrogation windows decreasing from 32 × 32 to 16 × 16 pixels with Gaussian weighting and 50% overlap. The average velocity field was obtained by averaging the velocity components at each spatial point for the 5 runs. The total error for the PIV measurements was estimated by evaluating PIV images with a known displacement. The RMS error is 0.03 of a pixel. Calibration error is approximately 0.2 pixels and the total error at $Re = 60,000$ is approximately 0.058 m s^{-1} or 12% at 3/4 span.

Vorticity fields were computed by taking the curl of the measured velocity field. This operation can amplify noise, and a nonlocal vortex detection scheme was used to identify vortex structures in the flow [19]. In this algorithm a scalar function γ at point P is defined as

$$\gamma(P) = \frac{1}{N}\sum_{S} \sin(\theta_M)$$

where S is a two-dimensional area centered on point P and N is the number of points inside S. θ_M is the angle between the radius vector from P to a point M that lies on S and the relative velocity vector at M, the total velocity at the point M minus the average velocity across the area S. γ is at its maximum when P is at the center of an axisymmetric vortex and is a measure of the vortex strength.

C. Dye Flow Visualization

Dye flow visualization was performed using a mixture of water, food coloring, and milk. Milk improves the stability of the dye filaments and is more reflective than food coloring alone [20]. The mass flow rate of dye injection was controlled by a syringe pump to ensure a constant flow of dye.

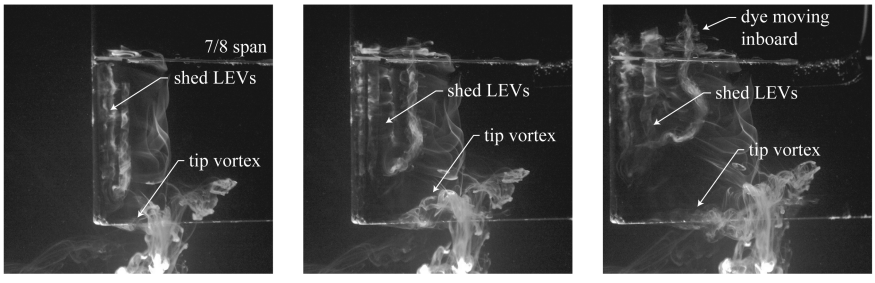

a) $\frac{x}{c}$ = 5.25 b) $\frac{x}{c}$ = 5.39 c) $\frac{x}{c}$ = 5.54

Fig. 12 Spanwise view of dye flow visualization from 7/8 span to the wing tip of the sliding wing at $Re = 10,000$, $\alpha = 25$ deg.

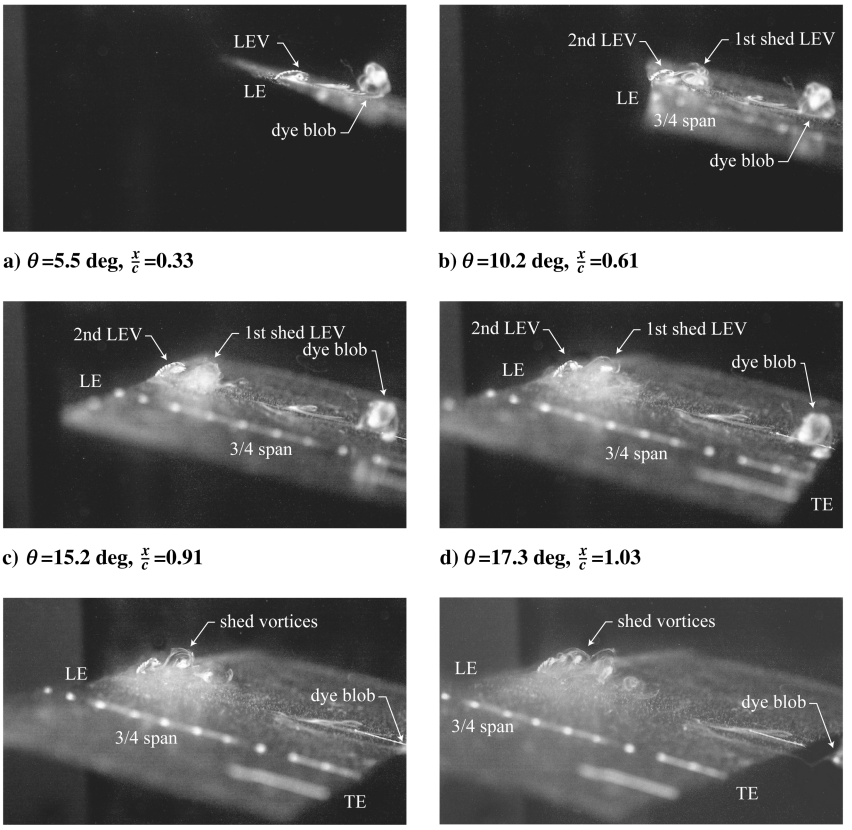

a) θ=5.5 deg, $\frac{x}{c}$=0.33 b) θ=10.2 deg, $\frac{x}{c}$=0.61

c) θ=15.2 deg, $\frac{x}{c}$=0.91 d) θ=17.3 deg, $\frac{x}{c}$=1.03

e) θ=18.2 deg, $\frac{x}{c}$=1.09 f) θ=19.4 deg, $\frac{x}{c}$=1.16

Fig. 13 Chordwise view of dye flow visualization on the waving wing at $Re = 10,000, \alpha = 25$ deg.

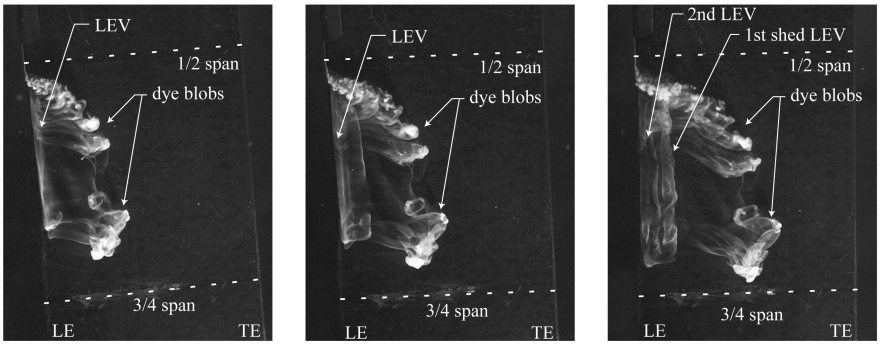

a) $\theta \approx$ 4 deg b) $\theta \approx$ 8 deg c) $\theta \approx$ 10 deg

Fig. 14 Spanwise view of dye flow visualization on the waving wing at $Re = 10,000, \alpha = 25$ deg.

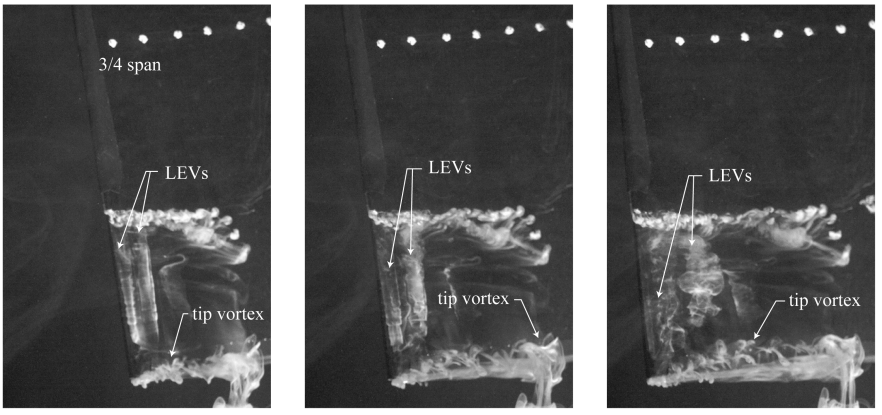

a) $\theta \approx$ 3 deg b) $\theta \approx$ 4 deg c) $\theta \approx$ 6 deg

Fig. 15 Spanwise view of dye flow visualization on the waving wing near the wing tip at $Re = 10,000, \alpha = 25$ deg.

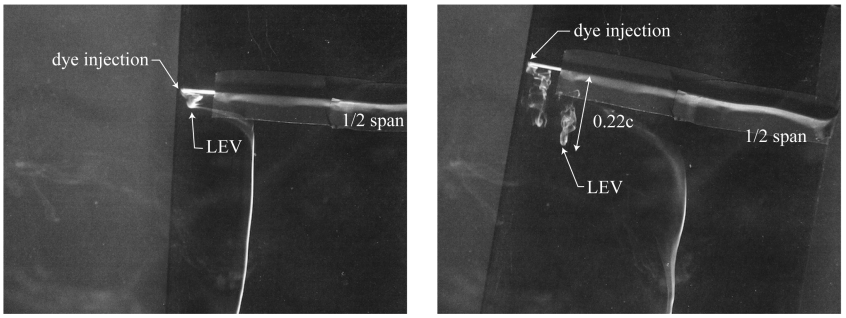

a) $\theta = 5.6$ deg b) $\theta = 12.2$ deg

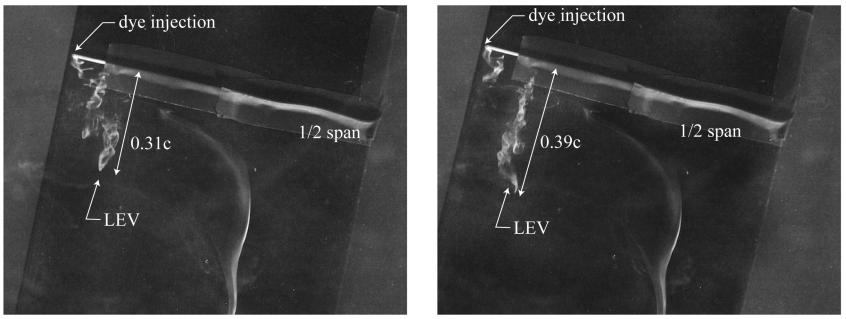

c) $\theta = 13.8$ deg d) $\theta = 15.3$ deg

Fig. 16 Spanwise view of dye flow visualization on the waving wing illustrating spanwise flow near 1/2 span at $Re = 10,000$, $\alpha = 25$ deg.

III. Results and Discussion

A. Flow Visualization on an Aspect Ratio 4 Sliding Wing

Figures 9 and 10 show dye flow visualization of an impulsively started aspect ratio 4 wing sliding from right to left at $Re = 10,000$ and a 25 deg angle of attack. Dye is injected on the suction side of the wing along the chord and the camera is located beyond the wing tip, providing a chordwise view of the flow. The blob of dye that starts at midchord is from dye injected before the wing motion began and is not a flow feature.

Figure 9 shows the flow near the beginning of the wing motion, in the first chord length of travel. Once the wing motion begins, flow quickly separates at the leading edge and a vortex forms in the separated region (Fig. 9b). This vortex continues to grow until it becomes too large to remain attached to the wing and separates past 0.6 chord lengths of travel (Fig. 9d). Flow is attached on the downstream portion of the wing as demonstrated by the motion of the dye blob along the wing surface. This region of attached flow is likely due to downwash generated by the starting vortex shed from the trailing edge.

As the wing motion continues, flow continues to separate at the leading edge and vortices continue to form and shed from the wing periodically. Vortex shedding continues throughout the wing motion as shown in Fig. 10. After the first LEV is shed, subsequent vortices appear to break off at a smaller size (Fig. 10d). The first LEV induces an upwash at the leading edge as it moves downstream. This upwash may cause subsequent leading-edge vortices to break off sooner, at a smaller size. Once multiple vortices extend along the wing surface the upwash at the leading edge becomes quasi steady and later vortices break off at similar sizes.

The sliding wing is the most two-dimensional experiment considered here, designed with a relatively high aspect ratio wing and two-dimensional kinematics. The spanwise flow visualization in Fig. 11 illustrates the two-dimensional nature of this flow. Dye is injected in a chordwise direction and is entrained in the shed leading-edge vortices. The dye diffuses outward in both directions towards the wing root and tip suggesting that there is no significant spanwise flow on the wing.

Nearer to the wing tip, the flow is more three-dimensional due to the formation of a tip vortex as shown in Fig. 12. Here the wing has traveled more than 5 chord lengths and the flow is nearing a quasi-steady state. Dye was injected at 7/8 span and at the wing tip well after

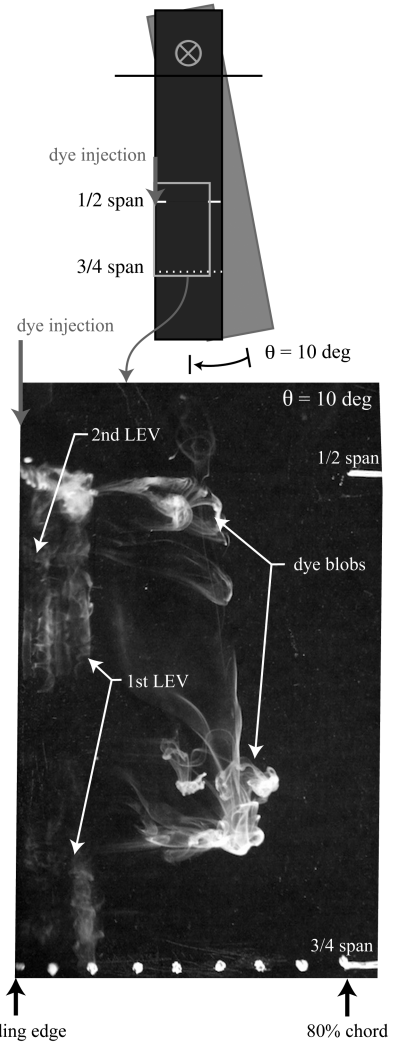

Fig. 17 Spanwise view of the waving wing after approximately 10 deg of rotation, $Re = 10,000$, $\alpha = 25$ deg.

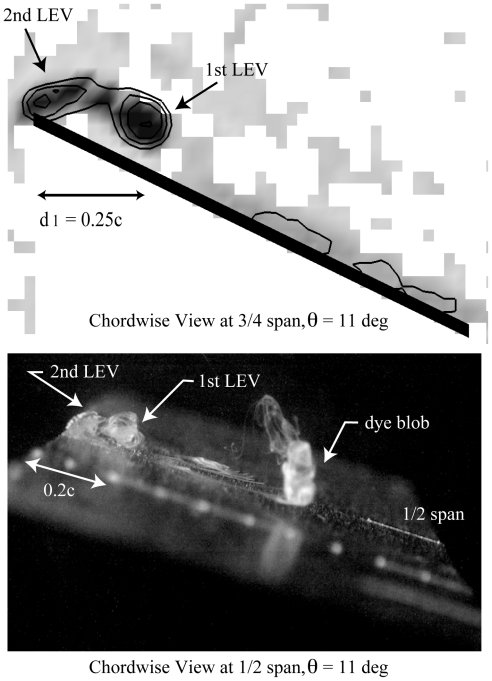

Fig. 18 Chordwise view of the waving wing after approximately 10 deg of rotation, $Re = 10,000$, $\alpha = 25$ deg.

the motion began. The wing passes through a cloud of dye at about $x/c = 5$ in order to visualize the leading-edge vortices in the region outboard of 7/8 span. A tip vortex is clearly visible, along with multiple leading-edge vortices that extend to very near the wing tip after 5.25 chord lengths of travel. Soon thereafter, the tip vortex occupies the outer portion of the wing and the leading-edge vortices are forced inboard. Even at 7/8 span, the flow is largely two-dimensional as evidenced by the dye diffusing inboard in Fig. 12c.

B. Flow Visualization on an Aspect Ratio 4 Waving Wing

Chordwise and spanwise views of the dye flow visualization on the waving wing are given in Figs. 13 and 14. In all of these images the aspect ratio 4 wing is waving from right to left at a Reynolds number of 10,000 and a 25 deg angle of attack. Dye was injected along the leading edge at half span. The 3/4 span plane is marked by a dotted line with dots approximately $0.10c$ apart. A blob is visible on the right side of the images due to dye injected before the wing motion starts and is not a flow feature. On the left side of the images, near the leading edge of the wing, a LEV is visible within the first 5 deg of the wing rotation (Figs. 13a and 14a). This vortex quickly sheds from the leading edge and by 8 deg of rotation there are two vortices visible (Figs. 13b and 14c). As the wing stroke progresses, vorticity is continuously generated and shed from the leading edge (Figs. 13d–13f). The frequency of vortex shedding appears to differ between the sliding and waving wings and is the subject of ongoing work.

Nearer to the wing tip, leading-edge vortices appear to form earlier in the wing stroke. In Fig. 15 dye is injected at 7/8 span and at the wing tip. Multiple leading-edge vortices are visible within the first 5 deg of the wing stroke. These shed leading-edge vortices extend well beyond 7/8 span to very near the tip vortex.

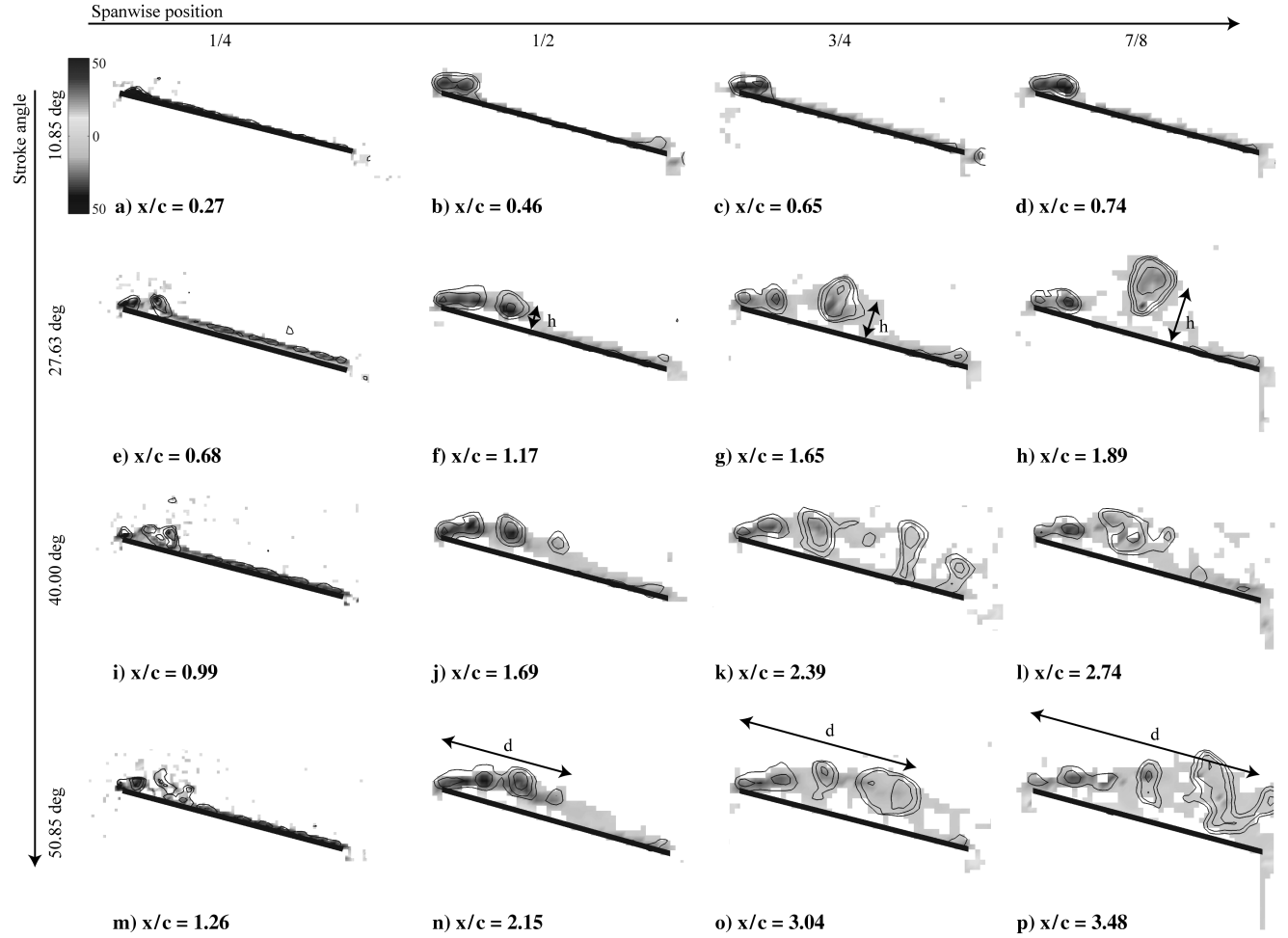

Fig. 19 Normalized vorticity fields on the aspect ratio 4 waving wing at $Re = 60,000$, $\alpha = 15$ deg. Each row represents the four stations on the wing at an instant in the wing stroke.

In Figs. 14 and 15 dye was injected towards the wing tip along the leading edge of the wing and thus it is not possible to draw firm conclusions regarding the spanwise flow along the waving wing. In Fig. 16 the dye is injected in a chordwise direction. Much less dye enters the core of the leading-edge vortices, but multiple vortices are still visible. Dye entrained in the first LEV moves downstream in a chordwise direction as well as in a spanwise direction towards the wing tip. From these images, the spanwise velocity of the dye in the first LEV can be estimated as approximately 0.05 m s^{-1}. The local wing velocity at this spanwise location is 0.06 m s^{-1}.

Figure 17 shows a typical spanwise view of the flow visualization at $Re = 10,000$ from 1/2 to 3/4 span after approximately 10 deg of the wing stroke. Dye is injected along the leading edge from the 1/2 span towards the wingtip. A corresponding chordwise view of the same flow is given in Fig. 18 using both flow visualization and PIV. The PIV data is shown as the vorticity field normalized by the local chordwise wing speed. Contours of the γ-function greater than 0.6 are overlaid in order to make the vortices in the flowfield more visible. This PIV analysis captures the structure of the flowfield well and is useful for visualizing and quantifying the flow at higher Reynolds numbers where large velocities make dye flow visualization more difficult.

An attached LEV was not observed on the waving wing despite the low Rossby number and the three-dimensional kinematics introduced through wing rotation. Previous experiments at Reynolds numbers $\mathcal{O}(1,000)$ report the formation of an attached LEV on flapping wings [2,6]. On a rotating wing, Lentink and Dickinson [8] observed a burst vortex that formed a less coherent region of recirculating flow but it remained attached to the wing. At higher Reynolds numbers, $Re = 8,000$, Tarascio et al. [21] observed periodically shedding vortices on a flapping wing. It appears that the development and stability of the LEV may be highly sensitive to Reynolds number and other experimental conditions.

C. PIV on an Aspect Ratio 4 Waving Wing

The flowfield around the waving wing was quantified using PIV at four spanwise locations on the wing: 1/4, 1/2, 3/4, and 7/8 span. PIV was performed at Reynolds numbers 10,000, 30,000, and 60,000 but because PIV error is generally a fixed value, higher flow speeds provide the highest signal to noise ratio. The quantitative analysis here is given for a Reynolds number of 60,000 and a more reasonable angle of attack for the higher Reynolds number, 15 deg.

Figure 19 shows chordwise slices of the normalized vorticity and γ-function for several points throughout the wing stroke. Each row of images shows four spanwise locations on the wing at a constant wing stroke angle θ with the wing moving from right to left. For each view, the vorticity field was computed by taking the curl of the velocity field as measured using PIV. The results are then normalized by the wing chord and local wing velocity at the spanwise plane of interest and values outside of the experimental error ($\epsilon_\omega = 4.7$ s^{-1}) are shown. All of the PIV data is shown using the same contour levels.

There are two differences in the behavior of the leading-edge vortices along the span. The first is the height of the shed vortices. The shed vortices appear to lift off the wing surface more quickly on the outboard sections of the wing. This is most apparent in Figs. 19e–19h, all at a stroke angle of $\theta = 27.63$ degs. At this point in the wing stroke the first shed vortex is clearly near the wing surface at 1/4 and 1/2 span but has lifted almost a core-diameter above the wing surface at 7/8 span.

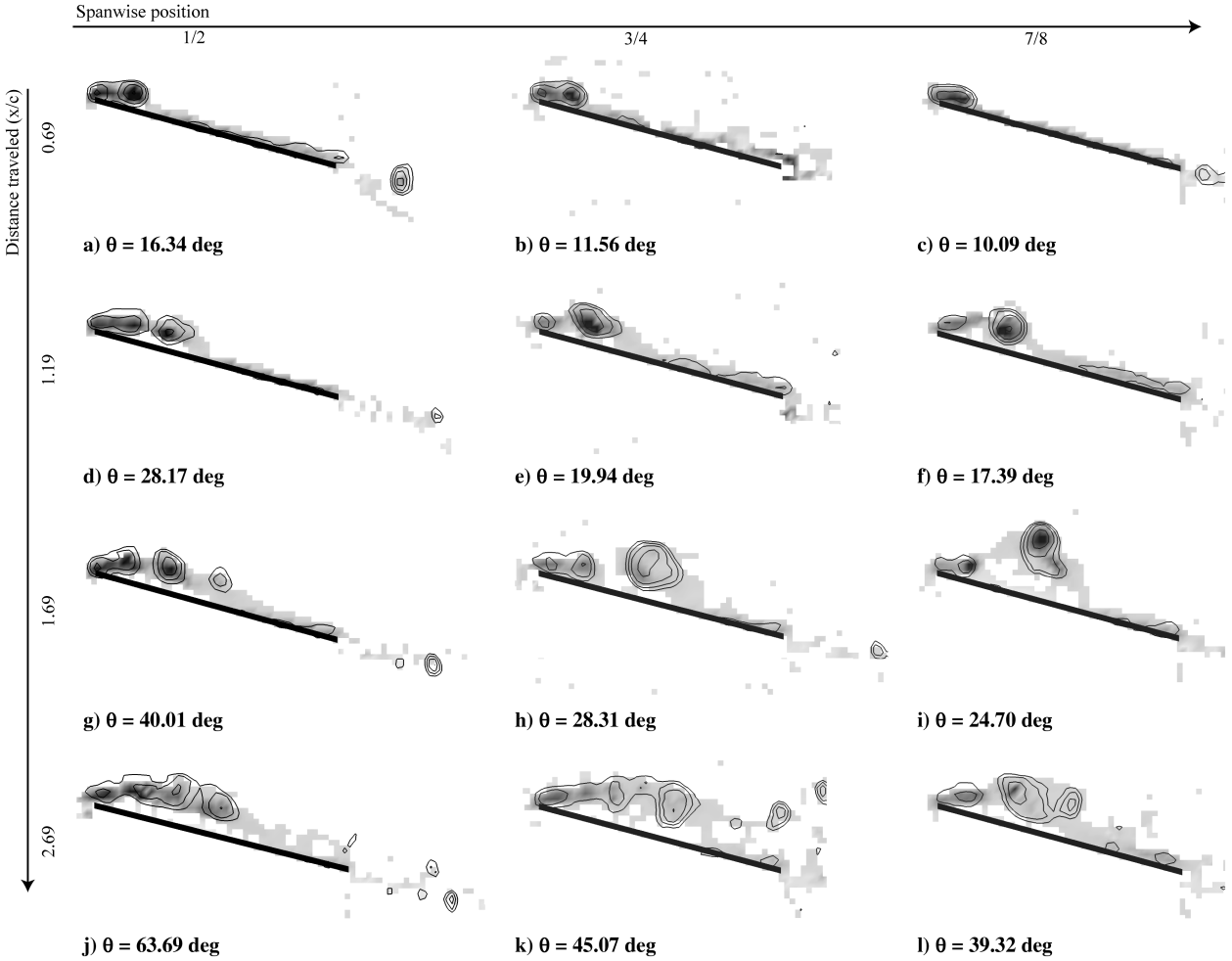

Fig. 20 Normalized vorticity fields on the aspect ratio 4 waving wing at $Re = 60,000$, $\alpha = 15$ deg. Each row represents three stations on the wing after traveling equivalent x/c distances.

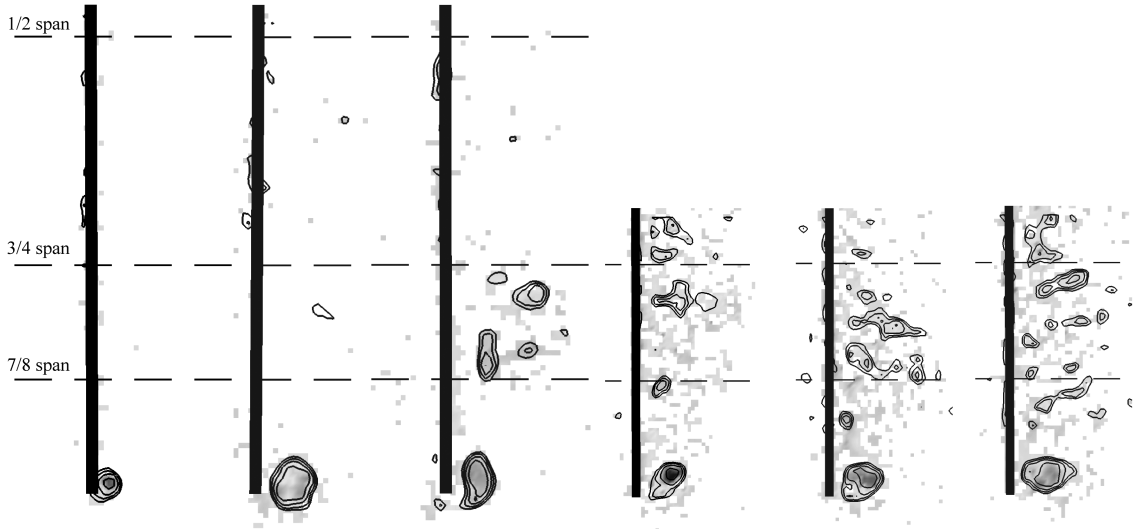

a) θ = 10.85 deg **b) θ = 27.63 deg** **c) θ = 40.00 deg** **d) θ = 50.85 deg** **e) θ = 67.63 deg** **f) θ = 80.00 deg**

Fig. 21 Spanwise view of the normalized vorticity fields at the trailing edge for AR = 4, $Re = 60,000$, $\alpha = 15$ deg.

Secondly, shed leading-edge vortices spread farther apart on the outboard sections. For example, four vortices are observed over the wing at a wing stroke angle $\theta = 50.85$ deg. These four vortices cover approximately half of the wing chord at 1/2 span. The same number of vortices stretch across 3/4 of the chord at 3/4 span and the vorticity extends past the trailing edge at 7/8 span. This could be because the wing tip has moved significantly farther than the wing root in terms of absolute distance. At a stroke angle of 50.85 deg the 1/2 span plane has traveled only 2.15 chord lengths whereas the 7/8 span plane has traveled 3.48 chord lengths.

Figure 20 shows the flowfield at three spanwise locations, this time after traveling the same absolute distance. The first row of images shows the 1/2, 3/4, and 7/8 span planes each having traveled 0.69 chord lengths, thus the 1/2 span plane has passed through a wing stroke angle of 16.34 deg whereas the 7/8 span plane has passed through only 10.09 deg. In this frame of reference the shed vortices are spread along the same streamwise distance at the different spanwise locations. Also, as was observed previously, shed vortices tend to lift further off of the wing surface on the outboard sections.

The spanwise view of the flowfield at the trailing edge of the wing is given in Fig. 21 and the flow in the wake is given in Fig. 22, 4.2 deg of rotation (a quarter-chord of travel at 3/4 span) behind the trailing edge. In all images, the wing is moving into the page and the suction side of the wing is to the right. Dashed lines mark the 1/2, 3/4, and 7/8 span planes. In this view the flow is characterized by the strong tip vortex that forms in the first 10 deg of the wing stroke and extends into the wake. Near $\theta = 45$ deg, a large region of vorticity on the upper surface of the wing appears at 3/4 span as the shed leading-edge vortices reach the trailing edge (Fig. 19k). The same happens at $\theta = 50.85$ deg when the leading-edge vortices at 7/8 span reach the trailing edge and appear in the spanwise view (Figs. 19p and 21d). This cloud of vorticity passes over the wing, ultimately forming a shear layer extending into the wake.

Figure 23 shows spanwise distributions of maximum local spanwise velocity above the wing surface normalized by the local freestream, $U' = \omega r$. There is a strong spanwise flow ($\approx$60% of the freestream) from wing root to tip after a wing stroke angle of about 45 deg which is not observed earlier in the wing stroke. In earlier waving wing experiments, spanwise flow was observed at 5% chord earlier in the wing stroke so there may be significant spanwise flow earlier in the wing stroke that does not appear in these measurements due to the time required for the flow to move from the leading edge to

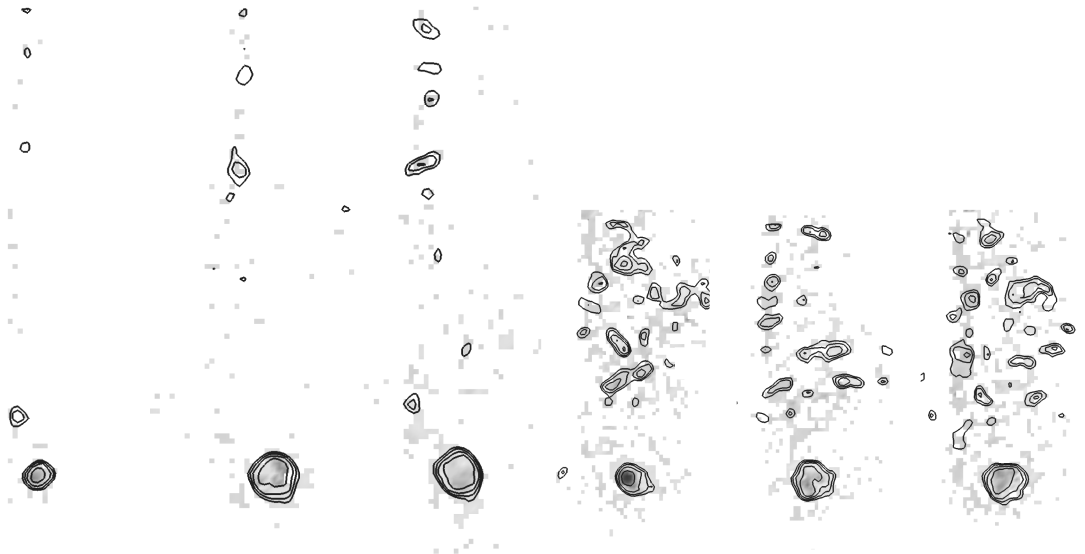

a) θ = 10.85 deg **b) θ = 27.63 deg** **c) θ = 40.00 deg** **d) θ = 50.85 deg** **e) θ = 67.63 deg** **f) θ = 80.00 deg**

Fig. 22 Spanwise view of the normalized vorticity fields in the wake 0.25*c* behind the trailing edge for AR = 4, $Re = 60,000$, $\alpha = 15$ deg.

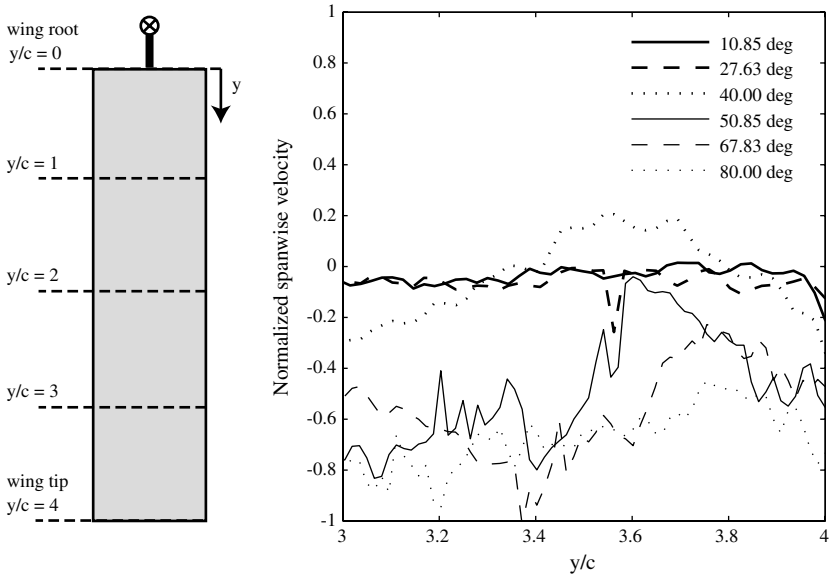

Fig. 23 Local spanwise velocities at the trailing edge normalized by the local freestream.

the trailing edge. This would be consistent with the dye flow visualization at $Re = 10,000$ given in Fig. 16.

D. PIV on an Aspect Ratio 2 Waving Wing

The angular velocity of the waving wing is directly related to the aspect ratio by $\omega = \nu Re/rc$ where $r = \frac{3}{4}\mathrm{AR}c + r_r$ and r_r is the distance from the axis of rotation to the wing root (Fig. 6). Since r_r is small, the rotational velocity required to achieve a given Reynolds number on the aspect ratio 2 wing is approximately twice that for the aspect ratio 4 wing. The lower aspect ratio wing is thus expected to have a steeper spanwise velocity gradient because higher angular velocities are required to achieve the same local Reynolds number.

Normalized vorticity fields for the aspect ratio 2 wing at $Re = 60,000$ and $\alpha = 15$ deg are given in Fig. 24. The fundamental structure of the flowfield appears to be the same as at aspect ratio 4. Although the flow over the aspect ratio 2 wing is expected to be more three-dimensional, a stable attached LEV is not observed. A vortex forms along the leading edge early in the wing stroke and sheds within the first 17 deg of rotation. As the wing stroke progresses a trail of shed vortices extends over the upper surface of the wing. The shed vortices move downstream through the wing stroke but have not yet reached the trailing edge of the wing at $\theta = 38.50$ deg. Like on the higher-aspect-ratio wing, vortices tend to spread further apart nearer the wing tip and shed vortices tend to lift off the wing surface near the wing tip, but remain close to the surface further inboard. This

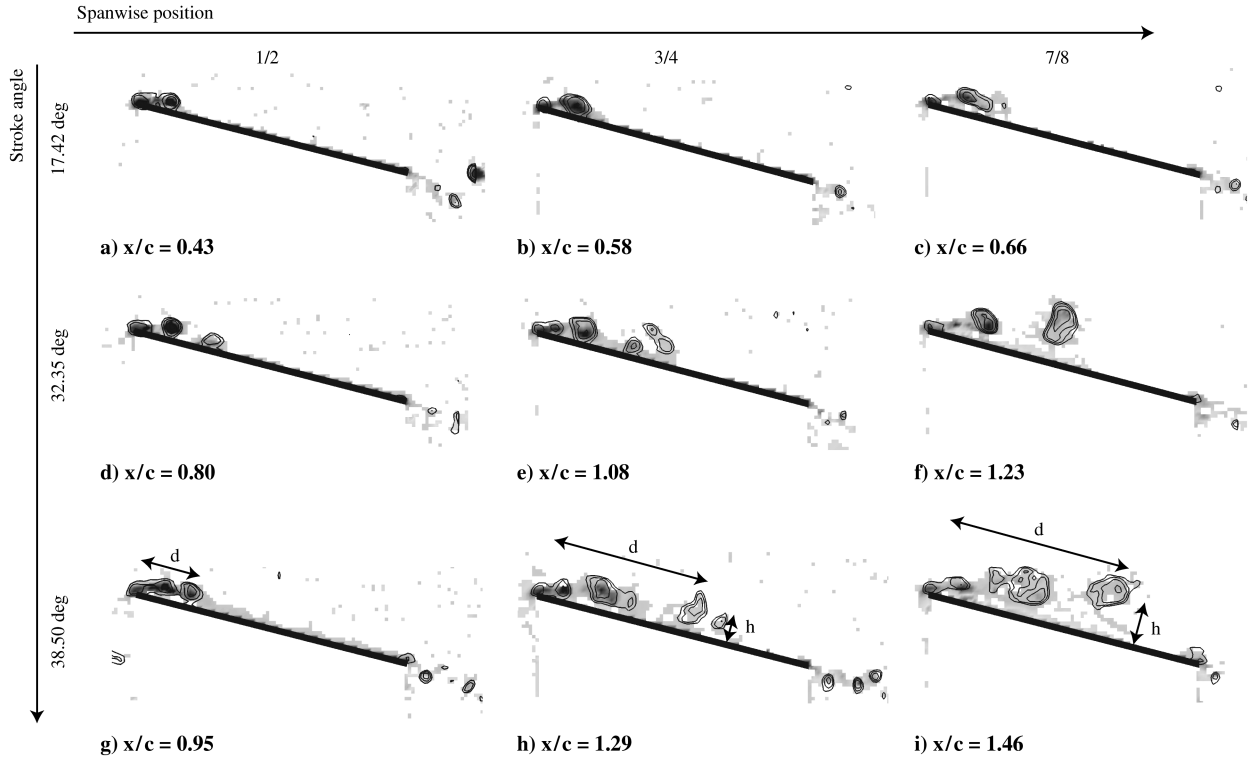

Fig. 24 Normalized vorticity fields on the aspect ratio 2 waving wing at $Re = 60,000, \alpha = 15$ deg. Each row represents the three stations on the wing at an instant in the wing stroke.

is most obvious between 1/2 and 3/4 span as shown in Figs. 24g and 24h.

IV. Conclusions

Three sets of experiments were performed increasing the three-dimensionality of the flow incrementally: an aspect ratio 4 sliding wing, an aspect ratio 4 waving wing, and an aspect ratio 2 waving wing. Dye flow visualization on the sliding and waving wings revealed the formation of unstable leading-edge vortices. PIV was used to quantify the spanwise flow on the waving wing and the growth of the LEV at multiple locations along the wing span.

On both the sliding and waving wings there is minimal interaction between the shed leading-edge vortices and the tip vortex. Spanwise flow has been observed on the waving wing but not on the sliding wing. Despite the increased three-dimensionality of the waving wing experiments, the structure of the flow appears to be largely two-dimensional over most of the wing span and is similar to that of the sliding wing. There is no evidence of a stably attached LEV on either the aspect ratio 4 or 2 waving wings.

The leading-edge vortices observed have a very high aspect ratio, extending along the entire length of the wing span with a diameter on the order of a tenth of the wing chord. These unstable vortices shed and move downstream, forming a trail of vortices over the surface of the wing. Towards the wing tip, shed vortices were observed to lift off of the wing surface but nearer the wing root vortices remain closer to the wing surface. At a given stroke angle the same number of vortices were observed along the length of the wing but cover a larger percentage of the wing chord near the wing tip than near the wing root, likely due to the higher wing speed near the tip. When normalized by absolute distance traveled, leading-edge vortices appear to develop more quickly further inboard and more shed vortices were observed near the wing root than near the wing tip.

Acknowledgments

The authors gratefully acknowledge financial support provided by the Air Force Research Laboratory European Office of Aerospace Research and Development Grant FA 8655-07-1-3082, Engineering and Physical Sciences Research Council, and the National Science Foundation.

References

[1] Ellington, C. P., "The Aerodynamics of Hovering Insect Flight, 4. Aerodynamic Mechanisms," *Philosophical Transactions of the Royal Society of London Series B, Biological Sciences*, Vol. 305, No. 1122, Feb. 1984, pp. 79–113. doi:10.1098/rstb.1984.0052

[2] Ellington, C. P., van den Berg, C., Willmott, A. P., and Thomas, A. L. R., "Leading-Edge Vortices in Insect Flight," *Nature*, Vol. 384, No. 6610, Dec. 1996, pp. 626–630. doi:10.1038/384626a0

[3] Sane, S. P., "The Aerodynamics of Insect Flight," *Journal of Experimental Biology*, Vol. 206, No. 23, Dec. 2003, pp. 4191–4208. doi:10.1242/jeb.00663

[4] van den Berg, C., and Ellington, C. P., "The Vortex Wake of a 'Hovering' Model Hawkmoth," *Philosophical Transactions of the Royal Society of London Series B, Biological Sciences*, Vol. 352, No. 1351, 1997, pp. 317–328. doi:10.1098/rstb.1997.0023

[5] van den Berg, C., and Ellington, C. P., "The Three-Dimensional Leading-Edge Vortex of a 'Hovering' Model Hawkmoth," *Philosophical Transactions of the Royal Society of London Series B, Biological Sciences*, Vol. 352, No. 1351, 1997, pp. 329–340. doi:10.1098/rstb.1997.0024

[6] Birch, J. M., Dickson, W. B., and Dickinson, M. H., "Force Production and Flow Structure of the Leading Edge Vortex on Flapping Wings at High and Low Reynolds Numbers," *Journal of Experimental Biology*, Vol. 207, No. 7, 2004, pp. 1063–1072. doi:10.1242/jeb.00848

[7] Ansari, S. A., Phillips, N., Stabler, G., Wilkins, P. C.,Żbikowski, R., and Knowles, K., "Experimental Investigation of Some Aspects of Insect-Like Flapping Flight Aerodynamics for Application to Micro Air Vehicles," *Experiments in Fluids*, Vol. 46, No. 5, April 2009, pp. 777–798. doi:10.1007/s00348-009-0661-2

[8] Lentink, D., and Dickinson, M. H., "Rotational Accelerations Stabilize Leading Edge Vortices on Revolving Fly Wings," *Journal of Experimental Biology*, Vol. 212, April 2009, pp. 2705–2719. doi:10.1242/jeb.022269

[9] Usherwood, J. R., and Ellington, C. P., "The Aerodynamics of Revolving Wings: 1. Model Hawkmoth Wings," *Journal of Experimental Biology*, Vol. 205, No. 11, 2002, pp. 1547–1564.

[10] Usherwood, J. R., and Ellington, C. P., "The Aerodynamics of Revolving Wings: 2. Propeller Force Coefficients from Mayfly to Quail," *Journal of Experimental Biology*, Vol. 205, No. 11, 2002, pp. 1565–1576.

[11] Wagner, H., "Über die Entstehung des dynamischen Äuftriebes von Tragflügeln," *Zeitschrift für Angewandie Mathematik und Mechanik*, Vol. 5, No. 1, 1925, pp. 17–35.

[12] Walker, P. B., "Growth of Circulation About a Wing and an Apparatus for Measuring Fluid Motion," Aeronautics Research Committee, Rept. 1402, 1931.

[13] Francis, R. H., and Cohen, J., "The Flow near a Wing Which Starts Suddenly from Rest and then Stalls," Aeronautical Research Council TR 1561, 1933, p. 90.

[14] Dickinson, M. H., and Götz, K. G., "Unsteady Aerodynamic Performance of Model Wings at Low Reynolds Numbers," *Journal of Experimental Biology*, Vol. 174, No. 1, Jan. 1993, pp. 45–64.

[15] Beckwith, R., and Babinsky, H., "Impulsively Started Flat Plate Flow," *Journal of Aircraft*, Vol. 46, No. 6, Nov.–Dec. 2009, pp. 2186–2188. doi:10.2514/1.46382

[16] Jones, A. R., and Babinsky, H., "Unsteady Lift Generation on Rotating Wings at Low Reynolds Numbers," *Journal of Aircraft*, Vol. 47, No. 3, 2010, pp. 1013–1021. doi:10.2514/1.46649

[17] Jones, A. R., "Unsteady Low Reynolds Number Aerodynamics of a Waving Wing," Ph.D. Thesis, Univ. of Cambridge, Cambridge, England, U.K., May 2010.

[18] Jones, A. R., and Babinsky, H., "Three-Dimensional Effects on a Waving Wing," 48th AIAA Aerospace Sciences Meeting and Exhibit, AIAA Paper 2010-0551, Orlando, FL, 4–7 Jan. 2010.

[19] Graftieaux, L., Michard, M., and Grosjean, N., "Combining PIV, POD and Vortex Identification Algorithms for the Study of Unsteady Turbulent Swirling Flows," *Measurement Science and Technology*, Vol. 12, No. 9, Aug. 2001, pp. 1422–1429. doi:10.1088/0957-0233/12/9/307

[20] Clayton, B., and Massey, B. S., "Flow Visualization in Water: A Review of Techniques," *Journal of Scientific Instruments*, Vol. 44, No. 1, 1967, pp. 2–11. doi:10.1088/0950-7671/44/1/302

[21] Tarascio, M. J., Ramasamy, M., Chopra, I., and Leishman, J. G., "Flow Visualization of Micro Air Vehicle Scaled Insect-Based Flapping Wings," *Journal of Aircraft*, Vol. 42, No. 2, March–April 2005, pp. 385–390. doi:10.2514/1.6055

[22] Beckwith, R. M. H., "An Impulsively Started Flat Plate Wing," Mphil, Univ. of Cambridge, Cambridge, England, U.K., 2008.